# Orbital angular momentum driven anomalous Hall effect

Oliver Dowinton [*] and Mohammad Saeed Bahramy [†]
*Department of Physics and Astronomy, The University of Manchester, Oxford Road, Manchester M13 9PL, United Kingdom*

(Received 23 January 2022; revised 29 April 2022; accepted 10 June 2022; published 28 June 2022)

Orbital angular momentum (OAM) plays a central role in regulating the magnetic state of electrons in nonperiodic systems such as atoms and molecules. In solids, on the other hand, OAM is usually quenched by the crystal field, and thus has a negligible effect on magnetization. Accordingly, it is generally neglected in discussions around band topology such as Berry curvature and intrinsic anomalous Hall effect (AHE). Here, we present a theoretical framework demonstrating that crystalline OAM can be directionally unquenched in transition metal oxides via energetic proximity of the conducting $d$ electrons to the local magnetic moments. We show that this leads to "composite" Fermi pockets with topologically nontrivial OAM textures. This enables a giant Berry curvature and a resultant intrinsic nonmonotonic AHE, even in collinearly ordered spin states. We use this model to explain the origin of the giant AHE observed in the forced ferromagnetic state of $EuTiO_3$ and propose it as a general scheme for OAM driven AHE.

DOI: 10.1103/PhysRevB.105.235142

## I. INTRODUCTION

The anomalous Hall effect (AHE) is a variant of the Hall effect that arises in magnetic conductors even in the absence of an external magnetic field. AHE has both extrinsic contributions, i.e., related to skew-scattering mechanisms, and intrinsic contributions, which are related to the geometric and topological properties of electronic states as formulated by Berry [1]. In a solid, we can treat the momentum space of the lattice, also known as the Brillouin zone (BZ), as a parameter space which in turn defines a manifold of electronic states that has a defined connection and curvature, commonly known as Berry connection and Berry curvature [2], respectively. Heuristically the Berry connection can be seen as the $k$-space dual of the magnetic potential, which gives us some intuition as to its connection to the AHE, and how we can have a Hall current in the absence of an external magnetic field. Berry curvature in a system can typically be attributed to energetically proximate energy eigenstates that are guaranteed by the symmetries and degrees of freedom of the system. Typically the focus is on degrees of freedom such as the spin or valley index, rather than orbital angular momentum (OAM), as the latter is usually quenched or of a trivial nature in solids.

Recently, the field of "orbitronics" has linked the orbital degree of freedom, and correspondingly OAM, to a variety of topological, and Hall current phenomena. This includes linking the valley Hall effect and or the spin Hall effect to an underlying orbital Hall effect [3–6], an orbitally driven (quantum) AHE [7–10], with direct links made to the underlying orbital ordering [7–9], and momentum space orbital textures, generated through an external electronic field or through lack of centrosymmetry, that result in Hall currents [4,11,12].

Building upon this, we present a framework for an externally controllable, orbitally driven AHE that arises from complex OAM textures. We examine a scenario in which the electronic structure possesses a collinear spin angular momentum (SAM) texture, but its OAM varies across the BZ due to orbital ordering from anisotropy externally imposed through a magnetic proximity effect. We show that the resulting OAM texture generates an emergent spin-orbit (SO) field that varies nontrivially over $k$ space, despite the collinearity of SAM, leading to composite Fermi pockets (energy isosurfaces of each band) with regions of different orbital character separated by sharp boundaries. This, in turn, generates a large OAM-dependent Berry curvature, dominating the contribution to the intrinsic AHE. Due to the topological nature of the OAM textures, the anomalous Hall conductivity, $\sigma_{xy}^{\mathrm{AHE}}$, is nonmonotonic with respect to the Fermi energy. As an example, we apply our model to the forced-ferromagnetic (FFM) phase of the rare-earth transition-metal oxide perovskite $EuTiO_3$. We show this system exhibits collinear SAM and noncollinear OAM, resulting from the applied magnetic field and energetic proximity of the Eu $4f$ and Ti $3d$ orbitals. This enables us to externally control the OAM induced Berry curvature, and resultant AHE, directly through the magnetic field orientation. Through this, we explore the Fermiology and Berryology of the low-energy bands, hosting the charge carriers, and find they are directionally warped by an Ruderman-Kittel-Kasuya-Yosida (RKKY) interaction between Eu $4f$ moments, mediated through Ti $3d$ states. This is shown to lead to an intrinsic nonmonotonic $\sigma_{xy}^{\mathrm{AHE}}$ that has been experimentally observed for $EuTiO_3$ but so far eluded rigorous explanation [13–15].

## II. COMPUTATIONAL METHODS

Bulk electronic structure calculations for $EuTiO_3$ and $SrTiO_3$ were performed within the density functional theory (DFT) using the Perdew-Burke-Ernzerhof exchange-correlation functional [16], as implemented in the WIEN2K

[*] oliver.dowinton@postgrad.manchester.ac.uk
[†] m.saeed.bahramy@manchester.ac.uk

 

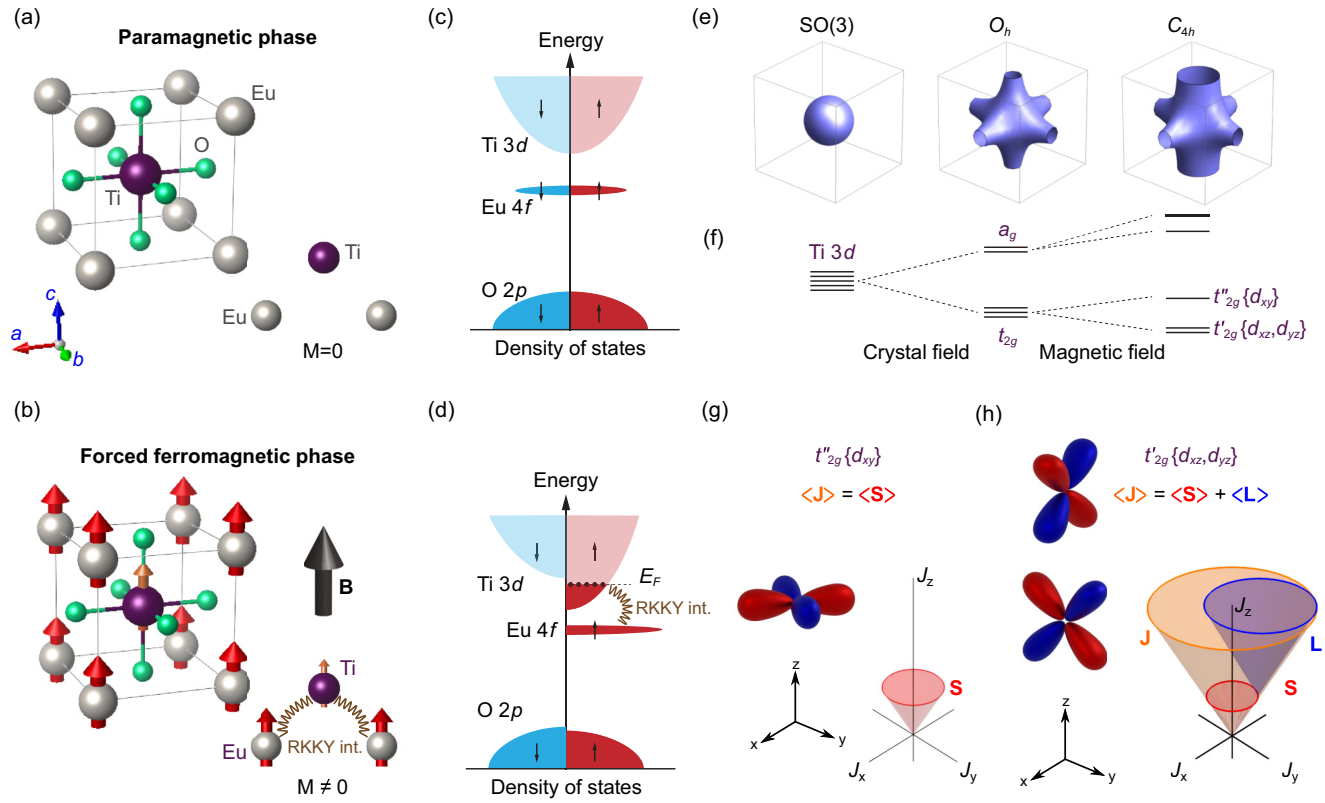


FIG. 1. (a) and (b) Magnetic configurations of $EuTiO_3$, in the paramagnetic (PM) and forced-ferromagnetic (FFM) phase, respectively. The external field is along the (001) direction. The insets in (a) and (b) show the corresponding RKKY interaction. (c) and (d) Schematic representations of the resulting density of states (DOS) in PM and FFM phases, respectively. (e) Model potentials, reflecting the symmetry reduction of the system. (f) Band diagram for Ti $3d$ states. (g), (h) Angular momentum in the system. (g) States with $d_{xy}$ orbital character have fully quenched OAM. (h) States formed from superpositions of $d_{xz}$, $d_{yz}$ have unquenched OAM, effectively uncoupled from SAM.

package [17]. Relativistic effects, including spin-orbit coupling, were fully taken into account. An effective Hubbard-like potential of $U_{\text{eff}} = 6$ eV for Eu was used to model the strong on-site Coulomb interaction of the Eu $4f$ states [18]. As discussed in Ref. [18], this correction can also treat the DFT's systematic misalignment of the conduction bands and their electronic dispersion at and well above the conduction band minimum. For both compounds, a cubic crystal structure with a lattice parameter of 3.905 Å was used. The corresponding BZ was sampled by a $10 \times 10 \times 10$ $k$ mesh. The lowest six conduction bands were then downfolded into a six-band tight-binding (TB) model using maximally localized Wannier functions [19,20] with the Ti $3d_{xy}$, Ti $3d_{yz}$ and Ti $3d_{xz}$ orbitals as the projection centers. The resulting TB wave function $|n(\mathbf{k})\rangle$ was finally used to compute the expectations values of spin angular momentum, $\langle n(\mathbf{k})|\widehat{\mathbf{S}}|n(\mathbf{k})\rangle \equiv \langle\widehat{\mathbf{S}}\rangle$, and orbital angular momentum, $\langle n(\mathbf{k})|\widehat{\mathbf{L}}|n(\mathbf{k})\rangle \equiv \langle\widehat{\mathbf{L}}\rangle$. From this the wave functions are used to compute $\sigma_{xy}^{\text{AHE}}$ as detailed in Wang *et al.* [21],

$$\sigma_{xy}^{\text{AHE}} = \frac{e^2}{\hbar}\frac{1}{N_k V_c}\sum_{\mathbf{k}}(-1)\Omega_z(\mathbf{k}),$$
$$\Omega_\alpha(\mathbf{k}) = \sum_n f_n(\mathbf{k})\Omega_{\alpha,n}(\mathbf{k}) \qquad (1)$$

where $\Omega_{\alpha,n}$ is the $\alpha = \{x, y, z\}$ component of the Berry curvature of Wannier band $n$,

$$\Omega_{\alpha,n} = -\epsilon_{\alpha\beta\gamma}\text{Im}\left[\left\langle\frac{\partial n}{\partial k_\beta}\middle|\frac{\partial n}{\partial k_\gamma}\right\rangle\right], \qquad (2)$$

where $\epsilon_{\alpha,\beta,\gamma}$ is the Levi-Civita tensor, $f_n$ is the Fermi-Dirac distribution, $\{\mathbf{k}\}$ is the sampling mesh, $N_k$ the size of the mesh, and $V_c$ the volume of the unit cell. The BZ integration of $\sigma_{xy}^{\text{AHE}}$ was carried out using a $200 \times 200 \times 200$ $k$ mesh adopting an additional $10 \times 10 \times 10$ subdivision within each volume increment wherever the Berry curvature was greater than 10 Å$^{-2}$.

## III. $EuTiO_3$ OVERVIEW

$EuTiO_3$ is a rare-earth perovskite [22] that has the novel property of separate conduction (Ti) and magnetic (Eu) centers, allowing it to possess both a high carrier mobility (in excess of 3000 cm$^2$ V$^{-1}$ s$^{-1}$ at 2 K) [18] and metamagnetism [23]. This metamagnetism arises out of a delicate competition between a superexchange antiferromagnetism (AFM) and an indirect ferromagnetic order through the Eu ions [24,25]. The system is naturally more stable in the weak AFM phase at temperatures below 5.5 K [26–28], which effectively can be regarded as a paramagnetic (PM) phase, as depicted in Fig. 1(a). Under a low magnetic field (2.1 T), $EuTiO_3$ transitions to an FFM order [18,29–31], as depicted in Fig. 1(b).

Forced ferromagnetism is distinguished from itinerant ferromagnetism, which is driven entirely by intrinsic exchange interactions, by the magnetic ordering arising from interactions between an external magnetic field and local magnetic centers, Eu $4f$ in our case. The Eu $4f$ sites do interact with each other through the Ti $3d$ conduction states in a double-exchange interaction, leading to a complete spin polarization of carriers for a broad range of carrier densities, as experimentally verified through magnetotransport measurements [18] for carriers up to $4 \times 10^{19}$ cm$^{-3}$. We have schematically illustrated the resulting change in the electronic structure from magnetization in Figs. 1(c) and 1(d).

The low-energy conduction bands here are dominated by the Ti $3d$–$t_{2g}$ states, i.e. $\{d_{xy}, d_{yz}, d_{xz}\}$ orbital submanifold, owing to the octahedral symmetry ($O_h$) of the host perovskite structure. Magnetizing the system along the (001) direction further splits the $t_{2g}$ states into two branches $t'_{2g}$ made of $\{d_{xz}, d_{yz}\}$ and $t''_{2g}$ made of $d_{xy}$ as depicted in Figs. 1(e) and 1(f) (which will be discussed in further detail later on). Due to this magnetic phase transition, these states undergo a tetragonal warping [15,18] despite the cubic symmetry of the crystal field. It should be noted that the crystal structure of cubic perovskites, such as $SrTiO_3$ and $EuTiO_3$, naturally deforms to a tetragonal phase due to lattice instabilities [32–35], which will induce an anisotropy that affects the $t_{2g}$ states. However, the directional distortions induced by the magnetic exchange will dominate the electronic properties of the $t_{2g}$ states over such a structural change. As such, first-principles calculations based on a cubic structure capture the experimentally measured Fermiology of FFM $EuTiO_3$ on a quantitative level, as detailed in Maruhashi *et al.* [18]. This magnetic distortion, as will be discussed later, is governed by a directional OAM operator $\widehat{\mathbf{L}}$, which, when added to the SAM operator $\widehat{\mathbf{S}}$, modifies the total angular momentum operator $\widehat{\mathbf{J}}$. However, as the exchange induced Zeeman splitting is an order of magnitude larger than the spin-orbit coupling (SOC) [see Figs. 2(a) and 2(b)], the $t_{2g}$ states are in the strong field regime and the OAM is effectively uncoupled from the SAM, such that $\widehat{\mathbf{J}} = \widehat{\mathbf{S}} + \widehat{\mathbf{L}}$, as shown in Figs. 1(g) and 1(h).

## IV. ELECTRONIC STRUCTURE

To aid the discussion, it is worthwhile comparing $EuTiO_3$ to its twin compound $SrTiO_3$, which shares the same crystal structure and similarly has high carrier mobility, but lacks any magnetic ordering [36–38]. In $SrTiO_3$, as $EuTiO_3$, the Ti $t_{2g}$ states form a conduction manifold close to the Fermi energy ($E_F$) [39,40]. As such, the $SrTiO_3$ $t_{2g}$ bands are analogous to those in undoped AFM $EuTiO_3$ where there is no net spin polarization. However, in $EuTiO_3$ the $Eu^{2+}$ $4f$ electrons form a nearly flat subgap manifold 0.5 eV from the conduction band minimum (CBM), with an admixture of O $2p$ and Ti $3d$ states [18,40], as shown in Fig. 2. By doping, we access the Ti $t_{2g}$ states which act as a mediator for an RKKY interaction between the Eu $4f$ states due to their energetic proximity [29,31] and the small admixture of Ti $3d$ states in the Eu $4f$ manifold. More precisely speaking, Eu $4f$ electrons are exchanged through the Ti $3d$ states with another Eu center, which is considerably "easier" if the spin of all three bands matches. As such, it is energetically favorable for the Eu $4f$ and Ti $3d$ states involved in the RKKY interaction to adopt the same direction of spin. With the application of an external magnetic field above 2.1 T, the $4f$ states align along the field and adopt an FFM order (spin up). Furthermore, the Ti $3d$ spin-up states are brought down in energy by the RKKY interaction, spin polarizing the $t_{2g}$ conduction states as shown schematically in Fig. 1(d), and as can be observed in the band structure in Fig. 3(a). Importantly, as the magnetic order arises from the "separate" Eu magnetic centers, the $t_{2g}$ states retain high mobility, and due to the localized nature of the $4f$ moments, we have direct control over the spin of the $t_{2g}$ states via manipulation of the applied magnetic field.

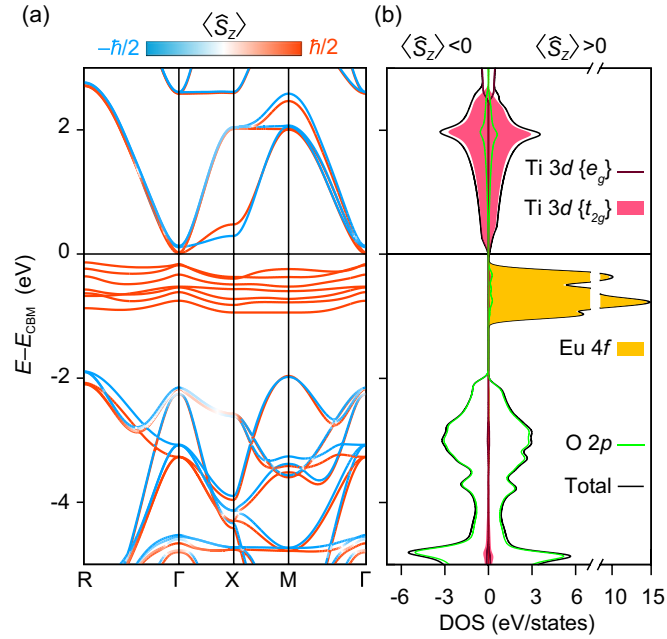


FIG. 2. (a) Spin-projected band structure of $EuTiO_3$ along the high-symmetry points of the Brillouin zone, energy offset against the conduction band minimum ($E_{CBM}$). (b) Spin-orbital-projected density of states (DOS) in the same energy window.

## V. ORBITAL-DEPENDENT DIRECTIONAL DISTORTION OF FERMI SURFACE

For the case of (001) magnetization, which is what is considered in Figs. 1 and 3, the $t_{2g}$ manifold near the CBM forms Fermi pockets with three distinct shapes [18] as shown in Fig. 3. The Fermi pockets intersect each other in the BZ, resulting in two distinct types of symmetry protected crossings in the $k_x$-$k_y$ plane [shown in Fig. 3(a)] that are topological features of the Berry curvature. The first type are Weyl nodes, occurring between states of opposite spin along $\Gamma \rightarrow X$. The second type, which are part of the titled nodal lines, are formed by states of the same spin but opposing orbital character along $\Gamma \rightarrow M$ and are protected by the planar mirror symmetry of $EuTiO_3$ [see Fig. 3(b)].

Figures 3(c)–3(k) show the orbital character, $\langle \widehat{\mathbf{S}} \rangle$, and $\langle \widehat{\mathbf{L}} \rangle$ projected onto the Fermi pockets at a typical carrier density where only the spin-up states are accessed, $n_c = 4 \times 10^{19}$ cm$^{-3}$ (corresponding to $E_F = 66$ meV). Here, we see distinct regions of different orbital character, a simple

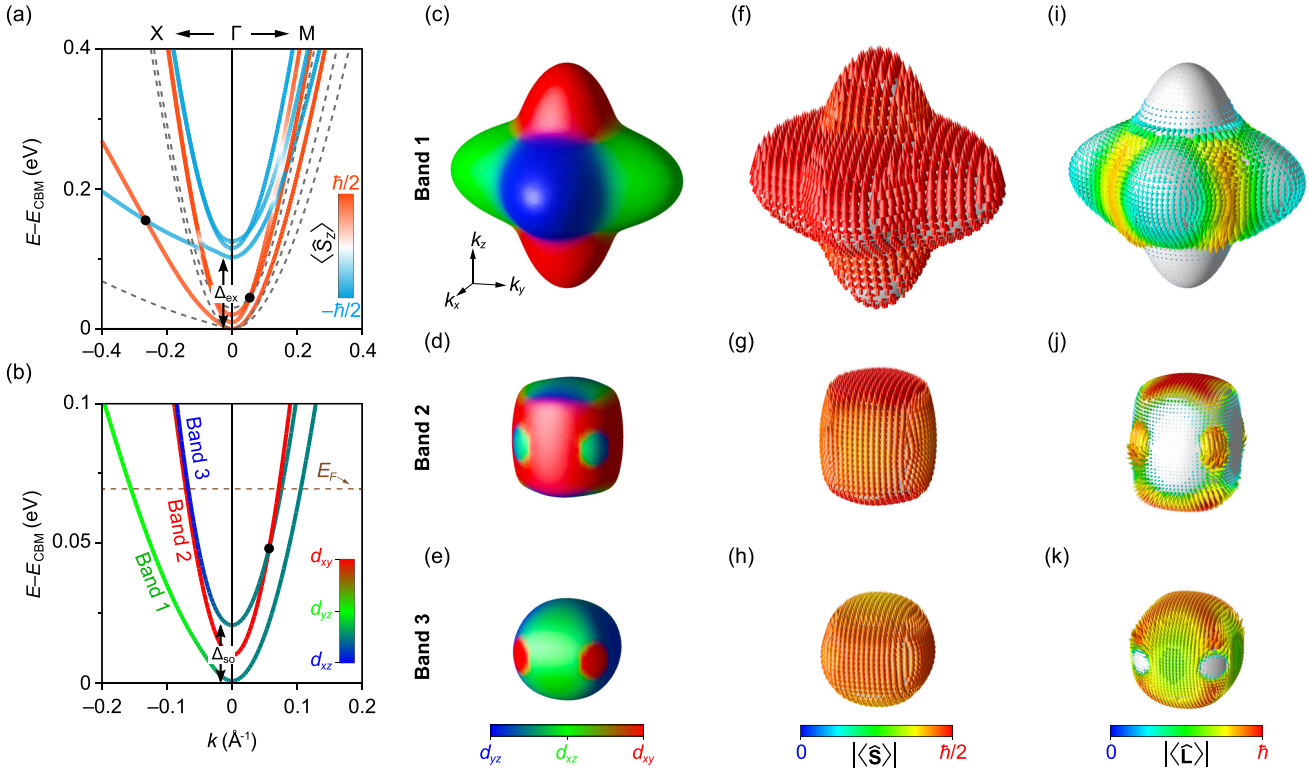


FIG. 3. (a) Low-energy electronic structures of FFM $EuTiO_3$ (solid lines) and $SrTiO_3$ (dashed). Black dots indicate the protected band crossings. (b) A magnified view of $EuTiO_3$ bands and their orbital characters. (c)–(e) The orbital character, (f)–(h) $\langle\widehat{\mathbf{S}}\rangle$, and (i)–(k) $\langle\widehat{\mathbf{L}}\rangle$ projected onto the resultant three Fermi pockets for a Fermi energy, $E_F$ indicated in (b), corresponding to a carrier density of $n_c = 4 \times 10^{19}$ cm$^{-3}$.

collinear spin texture, and regions with (un)quenched OAM. We show all three pockets accessed at this energy. However, we are primarily interested in the "light," more dispersive, second and third pockets as these will dominate transport properties. Given the collinearity of $\langle\widehat{\mathbf{S}}\rangle$, the behavior of the SO term $\widehat{\mathcal{H}}_{\mathrm{SO}} \propto \widehat{\mathbf{L}} \cdot \widehat{\mathbf{S}}$ must be entirely dependent on the OAM texture, which is in turn related directly to the orbital character. Specifically, in regions dominated by $d_{xy}$, $\langle\widehat{\mathbf{L}}\rangle$ is strongly suppressed.

The emergence of $\widehat{\mathcal{H}}_{\mathrm{SO}}$ leads to a characteristic compression and elongation of the second and third pockets along the $z$ direction, respectively. This contrasting behavior is due to the relative orientation of $\langle\widehat{\mathbf{S}}\rangle$ and $\langle\widehat{\mathbf{L}}\rangle$, which are antiparallel and parallel for the second and third pockets, respectively. Accordingly, the second pocket is lowered by $\langle\widehat{\mathcal{H}}_{\mathrm{SO}}\rangle$, thereby becoming more dispersive than the third pocket in the $k_x$-$k_y$ plane, manifesting as the above-mentioned directional distortions.

These distortions are quantified by the plot given in Fig. 4(a), where we can see how the cross-sectional area of the pockets varies with the angle of the plane of the cross section. Importantly, as these cross-sectional areas are directly related to the Shubnikov–de Haas oscillations in $EuTiO_3$, this Fermi-pocket warping is observable in any directional anisotropy of such oscillations [41,42]. To build up a clearer picture of $\widehat{\mathcal{H}}_{\mathrm{SO}}$ we consider its variation along the paths in $k$ space generated by the intersection of the FPs and the plane $k_x = k_y$ as shown in the right inset of Fig. 4. Such a path is captured by a single parameter, $\theta$, the angle of the intersecting in-plane $\mathbf{k}$ from the (0,0,1) direction. The magnitude of $\langle\widehat{\mathbf{L}}\rangle$, the $d_{xy}$ projection, and the corresponding $\langle\widehat{\mathcal{H}}_{\mathrm{SO}}\rangle$ along the path is shown in Figs. 4(c) and 4(e). For the warped pockets there is a sign change in $\langle\widehat{\mathcal{H}}_{\mathrm{SO}}\rangle$ moving from regions of a different orbital character due to the twisting of $\langle\widehat{\mathbf{L}}\rangle$, and the sign of the $\langle\widehat{\mathcal{H}}_{\mathrm{SO}}\rangle$ is opposite between each pocket on the top/bottom of the pockets as expected.

## VI. MECHANISM OF ORBITAL ANGULAR MOMENTUM QUENCHING

To understand the origin of noncollinear OAM it is worthwhile discussing the general symmetry properties and behavior of $d$ orbitals in perovskite structures. As already mentioned in Figs. 1(c) and 1(d), the crystal field in a cubic perovskite structure, subject to no external stimuli, reduces the continuous SO(3) symmetry of an electron around a free ion to $O_h$. The $3d$ orbitals, which are fivefold degenerate in free space, form two submanifolds corresponding to the $e_g\{x^2 - y^2, z^2\}$ and $t_{2g}\{xy, xz, yz\}$ irreducible representations of $O_h$. These manifolds are two- and threefold degenerate, respectively, but they are separated from each other by an energy gap, owing to the fact the $t_{2g}$ orbitals are farther from the ligands, and so experience less repulsion [43]. The angular component of these orbitals can be expressed in terms of cubic harmonics [44], i.e., as a sum of spherical harmonics $Y_l^m$ that reflects the symmetry of the lattice. Importantly, for $l = 2$, the

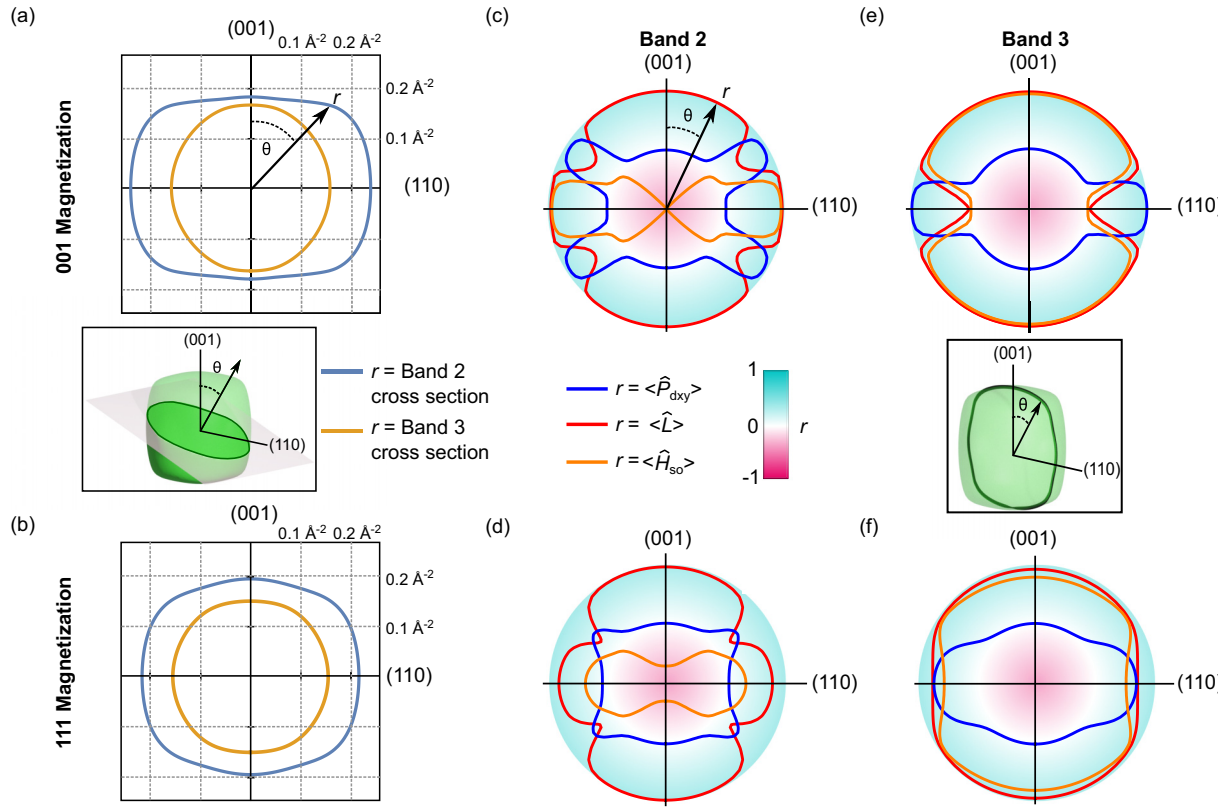


FIG. 4. (a) and (b) Cross-sectional area of second and third Fermi pockets for the (001) and (111) magnetization cases, respectively, where the angle specifies the normal of the cross-sectional plane as shown in the inset, and the radius specifies the area. (c)–(f) Evolution of $d_{xy}$ orbital projection ($\langle\widehat{P}_{d_{xy}}\rangle$), magnitude of OAM ($|\langle\widehat{\mathbf{L}}\rangle|$), and spin-orbit coupling $\langle\widehat{\mathcal{H}}_{\mathrm{SO}}\rangle$ over the path $\mathbf{k} = (0, 0, 1)$ to $\mathbf{k} = (1, 1, 0)$. Such a path is depicted, for an example, in the inset for the Fermi pocket of Band 2 under (001) magnetization. The plots go horizontally from Band 2 to Band 3, and vertically from (001) magnetization to (111). The radius corresponds to the expectation values in natural units, such that they lie in the interval $[-1, 1]$, and is shifted such that the origin corresponds to $r = -1$, so we can show the full range of the spin-orbit terms.

$t_{2g}$ manifold can be written explicitly as

$$\begin{aligned} d_{xy} &= \frac{i}{\sqrt{2}}\left(Y_2^{-2} - Y_2^2\right), \\ d_{xz} &= \frac{1}{\sqrt{2}}\left(Y_2^{-1} - Y_2^1\right), \\ d_{yz} &= \frac{i}{\sqrt{2}}\left(Y_2^{-1} + Y_2^1\right). \end{aligned} \tag{3}$$

Given that $\widehat{L}_z|Y_l^m\rangle = m|Y_l^m\rangle$, it is apparent for any state of the form

$$|X\rangle = \left|Y_l^m\right\rangle + e^{i\phi}\left|Y_l^{-m}\right\rangle, \tag{4}$$

where $\phi \in \mathbb{R}$,

$$\langle X|\widehat{L}_z|X\rangle = 0. \tag{5}$$

In addition, as $\widehat{L}_x$ and $\widehat{L}_y$ only mix $Y_l^m \to Y_l^{m\pm1}$, we can see that

$$\langle X|\widehat{L}_x|X\rangle = \langle X|\widehat{L}_y|X\rangle = 0, \tag{6}$$

implying that

$$\langle X|\widehat{\mathbf{L}}|X\rangle = \mathbf{0}. \tag{7}$$

As such, for the *unmixed* $t_{2g}$ states given in Eq. (3) $\langle\widehat{\mathbf{L}}\rangle = 0$, i.e., we say OAM has been quenched [45]. This can be anticipated from the $O_h$ symmetry, as there is no way to define a preferred direction for OAM.

### A. Orbital ordering for (001) magnetization

Magnetization along the $z$-axis (001) breaks the $O_h$ symmetry of the $EuTiO_3$, but importantly we retain a fourfold rotational symmetry in the $x$-$y$ plane. The generator of this rotation group is a rotation of $\frac{\pi}{2}$ about the $z$ axis. Hence to show a potential $\widehat{V}$ obeys this symmetry, it is sufficient to show it is invariant under such a $\frac{\pi}{2}$ rotation. If we expand our potential in terms of spherical harmonics,

$$\widehat{V} = \sum_{m,n=-l}^{l} V_{m,n}\left|Y_l^m\right\rangle\left\langle Y_l^n\right|, \tag{8}$$

we can see that after rotating we have

$$\widehat{V} \to \widehat{V}' = \sum_{m,n=-l}^{l} V_{m,n} e^{\frac{\pi}{2}(m-n)}|Y_l^m\rangle\langle Y_l^n|. \tag{9}$$

Hence, for $\widehat{V}$ to be invariant under such a rotation we have the requirement that $V_{m,n} \neq 0 \Rightarrow m = n$ or $m - n = \pm 4$. As such, the only off-diagonal terms are those that couple the $m = \pm 2$ harmonics. Furthermore, from the Hermiticity of $\widehat{V}$ and the property that $Y_2^2 = (Y_2^{-2})^*$, we have the results

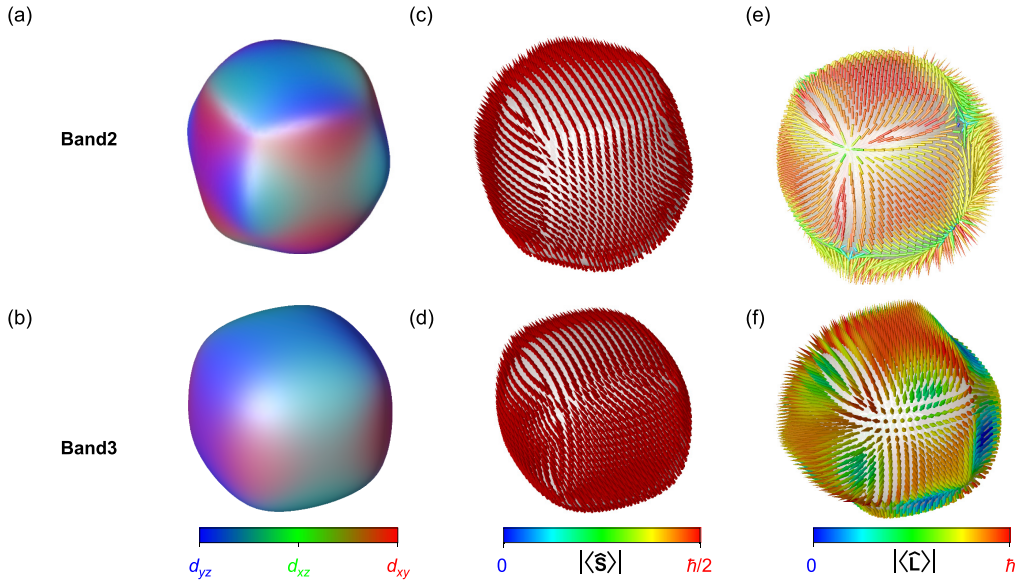


FIG. 5. Orbital character, $\langle\widehat{\mathbf{S}}\rangle$, and $\langle\widehat{\mathbf{L}}\rangle$ projected onto the Fermi pockets resulting from Band 2 and Band 3 (top and bottom rows, respectively) for the (111) magnetization.

$V_{2,-2} = V^*_{2,-2} = V^*_{-2,2} = V_{-2,2}$ and $V_{2,2} = V_{-2,-,2}$. Hence it is easy to show that the $d_{xy} = \frac{i}{\sqrt{2}}(Y_2^{-2} - Y_2^2)$ orbital is an eigenstate of $\widehat{V}$, as are the spherical harmonics $Y_2^{\pm 1}$. This analysis is directly related to the orbital angular momentum, as this generates the SO(3) rotation group, and so the $d_{xy}$ orbitals are distinct from the $\{d_{xz}, d_{yz}\}$ due to their fundamentally differing rotational symmetries.

Consequently, the $t_{2g}$ manifold is further split, with the $d_{xy}$ becoming separated from the $\{d_{xz}, d_{yz}\}$ orbitals which are degenerate along the high-symmetry planes $k_x = k_y$ due to their equivalent dispersion. Inclusion of $\langle\widehat{\mathcal{H}}_{\mathrm{SO}}\rangle$ will then open a gap, which in any multiorbital manifold will result in *some* orbital mixing. What is crucial here is that this degeneracy leads to a *perfect* orbital mixing between $\{d_{xz}, d_{yz}\}$ orbitals along these planes. Importantly, this explains the connection between $\langle\widehat{\mathbf{L}}\rangle$ and orbital character as shown in Fig. 3: Regions of a $d_{xy}$ character fully quench OAM, whereas regions with $\{d_{xz}, d_{yz}\}$ tend to retain it, with full unquenching along the $k_x = k_y$ planes where the $\{d_{xz}, d_{yz}\}$ states are perfectly mixed. Along such planes, $\langle\widehat{\mathbf{L}}\rangle$ can exceed $\langle\widehat{\mathbf{S}}\rangle$ by a factor of 2 and so comes to dominate the magnetization of the conducting states. As such, one can see that, given a multiorbital conduction manifold in the presence of SOC, the crystal symmetry considered is enough to unquench OAM due to the full orbital mixing.

Such a mixing arises from a real-space interorbital hopping between the $d_{xz}$ and $d_{yz}$ orbitals, which is facilitated by the same symmetry considerations above. Importantly, it has been shown that such off-diagonal interorbital hopping terms can lead to a large anomalous velocity, and so in the presence of anisotropy, such as our magnetic field, will generate a net AHE [46,47].

### B. Orbital ordering for (111) magnetization

From the above discussion one can infer how an external magnetic field could be used to control the OAM texture. To explore this, we consider magnetization along the (111) direction. This again breaks the octahedral symmetry, but retains the threefold rotational symmetry around this axis. Although it is not possible to give a full treatment of the crystal potential here, it is apparent that the $x$-$y$, $x$-$z$, and $y$-$z$ planes are all equivalent and so we do not expect large splitting between any of the $t_{2g}$ states, and so in turn do not expect any large quenching of OAM. Figures 4(d) and 4(f) confirm that there is less pronounced OAM quenching and less variation in $\langle\widehat{\mathcal{H}}_{\mathrm{SO}}\rangle$, leading to less distortion of the Fermi pockets [Fig. 4(b)]. Figure 5 shows that the symmetry properties of this magnetization lead to smoother boundaries between regions of orbital character, and importantly that the $d_{xy}$ orbitals are no longer isolated, leading to the less pronounced OAM quenching. $\langle\widehat{\mathbf{S}}\rangle$ is still collinear and now directed along (111). Hence, we have directly controlled the Fermiology, OAM texture, and spin direction by manipulating an external magnetic field.

## VII. BERRY CURVATURE

Each Fermi pocket exhibits sharp boundaries between the regions of different orbital characters for the (001) magnetization case. Hence these separate two distinct but energetically proximate eigenstates, leading to a large Berry curvature along these boundaries [2], that contributes to an intrinsic AHE [1,48]. Crucially, this Berry curvature arises due to a complex OAM texture because (as discussed previously) these "composite" Fermi pockets are generated by a varying $\langle\widehat{\mathcal{H}}_{\mathrm{SO}}\rangle$ field, despite a collinear SAM. To support this claim, we make an analytic link between OAM texture and Berry curvature

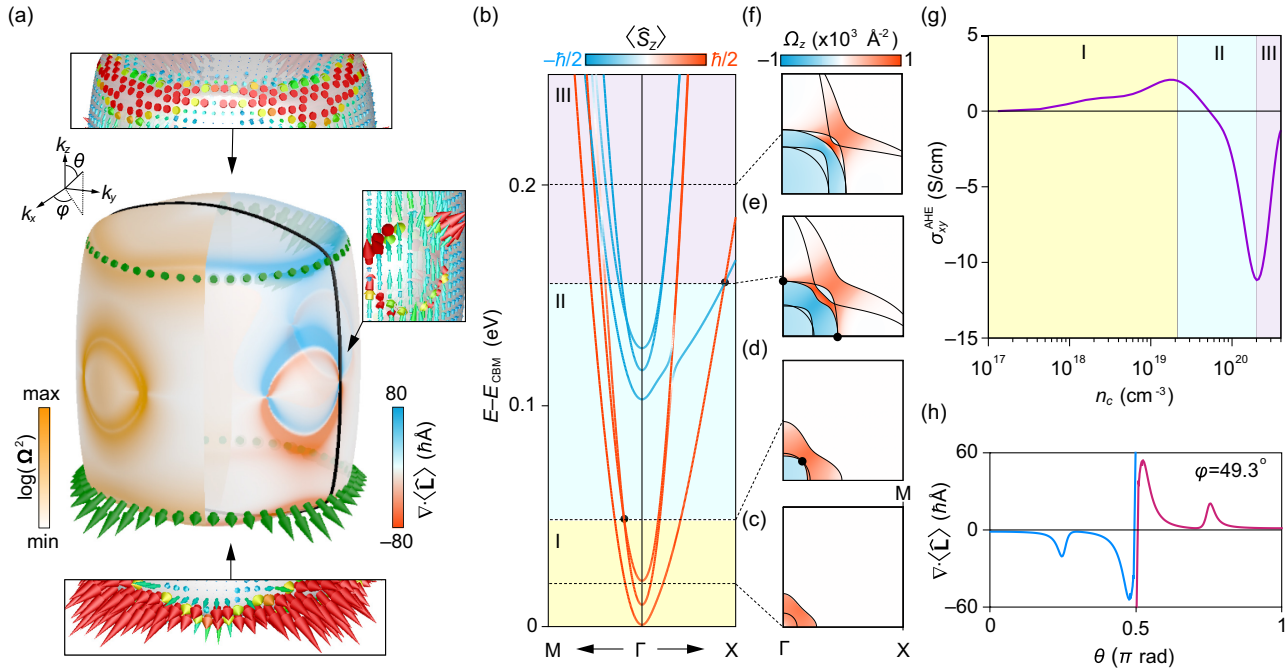


FIG. 6. Fermi pocket of Band 2 at $n_c = 4 \times 10^{19}$ cm$^{-3}$. The left-hand side shows Berry curvature magnitude from Eq. (13). The right-hand side shows divergence of OAM. Arrows show OAM on two paths along the top and bottom of the pocket, respectively. The insets show Berry curvature calculated numerically from Bloch states. (b) Reference band structure, with four Fermi energies marked corresponding to $n_c = 0.5, 2, 20, 50 \times 10^{19}$ cm$^{-3}$. (c)–(f) $z$ component of Berry curvature at said Fermi energies, taken in the $k_x$-$k_y$ plane with $k_x$ and $k_y$ varying from 0 to 0.15 $\pi/a$, where $a$ is the real-space lattice constant. Black dots mark symmetry protected crossings. (g) $n_c$ dependence of the $\sigma_{xy}^{\mathrm{AHE}}$. The shaded areas correspond to the energy windows shaded with the same colors in (b). (h) Divergence of OAM over path on the band 2 FP that passes through the nodal line [shown by the black line in (a)], where $\theta$ is the polar angle parametrizing the path.

that is easily computable. We start with the general expression for the Berry curvature originating from the $n$th energy eigenstate at $\mathbf{k}$, $|n(\mathbf{k})\rangle$ in the BZ,

$$\Omega_{\alpha,n} = -\epsilon_{\alpha\beta\gamma}\mathrm{Im}\left[\left\langle \frac{\partial n}{\partial k_\beta}\middle|\frac{\partial n}{\partial k_\gamma}\right\rangle\right], \tag{10}$$

which has a magnitude

$$|\boldsymbol{\Omega}_n(\mathbf{k})|^2 = \sum_{\alpha,\beta}\left(\left\langle \frac{\partial n}{\partial k_\alpha}\middle|\frac{\partial n}{\partial k_\beta}\right\rangle^2 - \left|\left\langle \frac{\partial n}{\partial k_\alpha}\middle|\frac{\partial n}{\partial k_\beta}\right\rangle\right|^2\right). \tag{11}$$

Given that $|n(\mathbf{0})\rangle$ is an eigenstate of $\widehat{\mathcal{H}}_{\mathrm{SO}}$, and that $\langle\widehat{\mathbf{S}}\rangle$ is collinearly ordered along the $\mathbf{z}$ direction, it must be an eigenstate of $\widehat{L}_z$. This allows us to approximate $|n(\mathbf{k})\rangle$ as being a small perturbation from an $\widehat{L}_z$ eigenstate for a range of $\mathbf{k}$ accessed by suitably small doping concentrations. This holds true in our scheme, as the primary Berry curvature features occur as boundaries between $d_{xy}$ and $\{d_{xz}, d_{yz}\}$ regions where the states are close to quantized, and the nodal lines $\Gamma \to \mathrm{M}$ where the mirror symmetry and band degeneracy give perfect $\widehat{L}_z$ eigenstates. From this, it can be shown that around key Berry curvature features

$$\frac{\partial}{\partial k_\beta}\left(\frac{1}{\lambda_n}\frac{\partial \lambda_n}{\partial k_\alpha}\right) \propto \mathrm{Re}\left[\left\langle \frac{\partial n}{\partial k_\alpha}\middle|\frac{\partial n}{\partial k_\beta}\right\rangle\right], \tag{12}$$

where $\lambda_n \equiv \langle n|\widehat{L}_z|n\rangle$. The full derivation of this term can be found in Appendix C. Putting Eqs. (11) and (12) together,

$$|\boldsymbol{\Omega}_n(\mathbf{k})|^2 \propto \sum_{\alpha,\beta}\left(\frac{\partial}{\partial k_\beta}\left(\frac{1}{\lambda_n}\frac{\partial \lambda_n}{\partial k_\alpha}\right)\right)^2 - \frac{\partial}{\partial k_\beta}\left(\frac{1}{\lambda_n}\frac{\partial \lambda_n}{\partial k_\alpha}\right)\frac{\partial}{\partial k_\alpha}\left(\frac{1}{\lambda_n}\frac{\partial \lambda_n}{\partial k_\beta}\right). \tag{13}$$

This term is plotted explicitly for the second pocket in the left-hand side of Fig. 6(a). Comparing it with the total $\boldsymbol{\Omega}_n(\mathbf{k})$ directly calculated from the Bloch wave functions [see the insets in Fig. 6(a)], we find a good agreement. This accordingly confirms the link between OAM texture and Berry curvature.

## VIII. ORBITAL ANGULAR MOMENTUM DRIVEN ANOMALOUS HALL EFFECT

The OAM texture and its topological nature is further elucidated in the right-hand side of Fig. 6(a). For the second Fermi pocket, we can see that the $k_z = 0$ plane separates regions with a negative/positive OAM divergence, $\nabla_{\mathbf{k}} \cdot \langle\widehat{\mathbf{L}}\rangle$, above/below it, respectively. Hence, the OAM "flows" from the bottom half, which acts as a source, to the upper half as a sink. The direction of this flow characterizes the OAM texture type, and is opposite for the third Fermi pocket compared to the first two. The OAM itself is also depicted along the top and bottom of the pocket, to reinforce the pole/antipole-like behavior of $\langle\widehat{\mathbf{L}}\rangle$ in these regions.

### A. Anomalous Hall conductivity

The Berry curvature contributes to an intrinsic AHE as follows,

$$\sigma_{xy}^{\mathrm{AHE}} = -\frac{e^2}{\hbar}\sum_n \int_{\mathrm{BZ}} f[E_n(\mathbf{k})]\Omega_{z,n}(\mathbf{k})\frac{d\mathbf{k}}{(2\pi)^3} \tag{14}$$

where $f$ is the Fermi-Dirac distribution, and the integral is across the entire BZ [1]. Increasing $E_F$, we expect a systematic evolution in the magnitude and sign of $\Omega_{z,n}(\mathbf{k})$ as we access different OAM texture types. We focus on the $z$ component of $\mathbf{\Omega}$ as the $x$ and $y$ components will have vanishing integrals over the BZ due to the rotational symmetry of the system, hence they do not contribute towards the AHE. Starting from the CBM, where only the first and second pockets (which are of the same OAM character) are present, the occupied states in the BZ carry a giant positive $\Omega_z(\mathbf{k})$, which in turn leads to a positive $\sigma_{xy}^{\mathrm{AHE}}$ growing monotonously with increasing $E_F$ [compare Figs. 6(b), 6(c) and 6(g)]. Once $E_F$ crosses the third pocket, a new region with a negative $\Omega_z(\mathbf{k})$ contribution emerges due to opposite OAM character of the second pocket [see Fig. 6(d)]. The competition between these two regions reaches its critical point at the protected crossing between the second and third pocket along the $\Gamma \rightarrow$ M direction, bringing $\sigma_{xy}^{\mathrm{AHE}}$ to its peak, as highlighted by the region I shaded in yellow in Fig. 6(g). Further increasing $E_F$ leads to the domination of the negative $\Omega_z(\mathbf{k})$ contribution, manifested by a sign change in $\sigma_{xy}^{\mathrm{AHE}}$ for $n_c \sim 2 \times 10^{19}$ cm$^{-3}$ [cyan region II in Fig. 6(g)]. This trend continues until $E_F$ crosses the Weyl node along the $\Gamma \rightarrow$ X direction at $n_c \sim 2 \times 10^{20}$ cm$^{-3}$. At this point $\sigma_{xy}^{\mathrm{AHE}}$, which is now negative, shows another turning point and begins to increase, as depicted in the purple region III in Fig. 6(g).

Such an $n_c$-dependent sign change in $\sigma_{xy}^{\mathrm{AHE}}$ is consistent with the previous experimental observations [13–15]. In particular, a comparison to the experimental results of $\sigma_{xy}^{\mathrm{AHE}}$ presented in Fig. 4(D) of Takahashi *et al.* [14] shows great agreement between our calculations and real life measurements, except for an overall sign difference, as the experimental measurements are sensitive to the carrier charge, which is negative here due to the electron-type carriers. Nevertheless, our calculations demonstrate that the observed intrinsic $\sigma_{xy}^{\mathrm{AHE}}$ can be well described by such complex, topological OAM textures.

### B. Topology of OAM texture

To elaborate on the role of the $\Gamma \rightarrow$ M protected crossings in the Berry curvature, and how this relates to the OAM texture, we note that these are part of a nodal line in the $k_x$-$k_y$ plane that begins along this direction, and at our plotted carrier density ($4 \times 10^{19}$ cm$^{-3}$) intersects the Fermi pocket as a pair of protected crossings, which we expect to be topological features of the Berry curvature, acting as quantized monopoles. At this $n_c$, one of these crossings occurs at an azimuthal angle $\phi = 49.3^\circ$ from the $k_x$ axis. Considering $\nabla_{\mathbf{k}} \cdot \langle \widehat{\mathbf{L}} \rangle$ over a path [shown as a black line in Fig. 6(a) on the Fermi pocket] that intersects this crossing [Fig. 6(h)] we can see that it becomes nonanalytic at the degeneracy, showing these are as much topological features of the OAM texture as they are of the Berry curvature. Hence the inclusion of the nodal line, and thus moving between regions I and II of $\Omega_z$, corresponds directly to a change in OAM texture for the Fermi pockets.

## IX. CONCLUSION

In conclusion, externally imposed anisotropies on systems with complex orbital manifolds, through energetic proximity to magnetic centers, can directionally unquench OAM. The resulting nontrivial, topological OAM textures can generate large Berry curvature, with an intrinsic orbital AHE, even in systems with collinear spin textures. In discussing OAM in $EuTiO_3$, we explained previous observations of warped Fermiologies and a nonmonotonic $\sigma_{xy}^{\mathrm{AHE}}$ as arising from $k$-space varying OAM. Given the ubiquity of transition-metal perovskites, and orbitally complex systems in general, our analysis forms a simple, general platform for an orbitronic AHE that is easily controlled due its dependence on imposed anisotropies. Finally, we hope our analysis has highlighted the role of OAM textures in orbitally driven AHE.

## ACKNOWLEDGMENTS

The authors gratefully acknowledge the Research Infrastructures at the University of Manchester for allocations on the CSF3 high performance computing facilities. M.S.B. is thankful to D. Maryenko, K. Takahashi, and M. Kawasaki for fruitful discussions.

## APPENDIX: BERRY CURVATURE TERM DERIVATION

Here, we detail the full derivation of the expression relating OAM texture to the Berry curvature of the Brillouin zone (BZ) as discussed in the main text. For the $n$th energy eigenstate at $\mathbf{k}$, $|n(\mathbf{k})\rangle$, consider the general expression for its contribution to the Berry curvature over a three-dimensional (3D) BZ ($\mathbf{k}$ dependence of $|n\rangle$ is implicit from now on),

$$\Omega_{\alpha,n} = -\epsilon_{\alpha\beta\gamma}\mathrm{Im}\left[\left\langle \frac{\partial n}{\partial k_\beta}\middle|\frac{\partial n}{\partial k_\gamma}\right\rangle\right], \tag{A1}$$

and use the standard vector algebra identity $\epsilon_{\alpha\beta\gamma}\epsilon_{\alpha\zeta\eta} = \delta_{\beta\zeta}\delta_{\gamma\eta} - \delta_{\beta\eta}\delta_{\gamma\zeta}$ to write its magnitude

$$|\mathbf{\Omega}_n(\mathbf{k})|^2 = \sum_{\alpha,\beta}\left(\left\langle \frac{\partial n}{\partial k_\alpha}\middle|\frac{\partial n}{\partial k_\beta}\right\rangle^2 - \left|\left\langle \frac{\partial n}{\partial k_\alpha}\middle|\frac{\partial n}{\partial k_\beta}\right\rangle\right|^2\right). \tag{A2}$$

We can then relate this to OAM as follows: First, consider that the energy eigenstates must be eigenstates of $\widehat{\mathcal{H}}_{\mathrm{SO}}$ at the gamma point, and given that at low energies the spin is entirely collinear along $z$ this means that more specifically they are eigenstates of $\widehat{L}_z$. Hence we make the approximation that for a range of $\mathbf{k}$ our states are close to eigenstates of $\widehat{L}_z$ such that we remove off-diagonal terms:

$$\widehat{L}_z|n\rangle = C_n|n\rangle + \sum_{m\neq n} C_m|m\rangle \approx C_n|n\rangle \equiv \lambda_n|n\rangle. \tag{A3}$$

As the OAM texture arises from the changing orbital character of the energy eigenstates and not any $k$-space variation in the OAM operator itself, it is clear that

$$\langle n|\nabla_{\mathbf{k}}\widehat{L}_z|n\rangle = \mathbf{0}. \tag{A4}$$

Combining Eqs. (A3) and (A4), and taking the **k** dependence of $\lambda_n$ to be implicit,

$$\begin{aligned}\frac{\partial\lambda_n}{\partial k_\alpha} &= \int\left[\frac{\partial n^*}{\partial k_\alpha}\widehat{L}_z n + n^*\frac{\partial\widehat{L}_z}{\partial k_\alpha}n + n^*\widehat{L}_z\frac{\partial n}{\partial k_\alpha}\right]d\mathbf{r}^3\\ &= \int\left[n^*\widehat{L}_z\frac{\partial n}{\partial k_\alpha} - \left(\frac{\partial n}{\partial k_\alpha}\right)^*\widehat{L}_z n\right]d\mathbf{r}^3\\ &= \langle n|\widehat{L}_z\left|\frac{\partial n}{\partial k_\alpha}\right\rangle - \left\langle\frac{\partial n}{\partial k_\alpha}\right|\widehat{L}_z|n\rangle\\ &= \lambda_n\left(\left\langle n\left|\frac{\partial n}{\partial k_\alpha}\right\rangle - \left\langle\frac{\partial n}{\partial k_\alpha}\right|n\right\rangle\right),\end{aligned} \tag{A5}$$

where we have used the anti-Hermitian property of $\partial_{k_i}$. From this we write

$$\begin{aligned}\frac{\partial}{\partial k_\beta}\left(\frac{1}{\lambda_n}\frac{\partial\lambda_n}{\partial k_\alpha}\right) &= \left\langle\frac{\partial n}{\partial k_\alpha}\middle|\frac{\partial n}{\partial k_\beta}\right\rangle + \left\langle\frac{\partial n}{\partial k_\beta}\middle|\frac{\partial n}{\partial k_\alpha}\right\rangle\\ &\quad - \left\langle\frac{\partial^2 n}{\partial k_\alpha\partial k_\beta}\middle|n\right\rangle - \left\langle n\middle|\frac{\partial^2 n}{\partial k_\alpha\partial k_\beta}\right\rangle\\ &= 4\mathrm{Re}\left[\left\langle\frac{\partial n}{\partial k_\alpha}\middle|\frac{\partial n}{\partial k_\beta}\right\rangle\right],\end{aligned} \tag{A6}$$

Hence,

$$\begin{aligned}|\boldsymbol{\Omega}_n(\mathbf{k})|^2 \propto \sum_{\alpha,\beta}&\left(\frac{\partial}{\partial k_\beta}\left(\frac{1}{\lambda_n}\frac{\partial\lambda_n}{\partial k_\alpha}\right)\right)^2\\ &- \frac{\partial}{\partial k_\beta}\left(\frac{1}{\lambda_n}\frac{\partial\lambda_n}{\partial k_\alpha}\right)\frac{\partial}{\partial k_\alpha}\left(\frac{1}{\lambda_n}\frac{\partial\lambda_n}{\partial k_\beta}\right).\end{aligned} \tag{A7}$$


[1] N. Nagaosa, J. Sinova, S. Onoda, A. H. MacDonald, and N. P. Ong, Rev. Mod. Phys. **82**, 1539 (2010).
[2] M. V. Berry, Proc. R. Soc. London, Ser. A **392**, 45 (1984).
[3] D. Xiao, W. Yao, and Q. Niu, Phys. Rev. Lett. **99**, 236809 (2007).
[4] D. Go, D. Jo, H.-W. Lee, M. Kläui, and Y. Mokrousov, Europhys. Lett. **135**, 37001 (2021).
[5] S. Bhowal and G. Vignale, Phys. Rev. B **103**, 195309 (2021).
[6] T. P. Cysne, M. Costa, L. M. Canonico, M. B. Nardelli, R. B. Muniz, and T. G. Rappoport, Phys. Rev. Lett. **126**, 056601 (2021).
[7] M. Zhang, H.-h. Hung, C. Zhang, and C. Wu, Phys. Rev. A **83**, 023615 (2011).
[8] G.-F. Zhang, Y. Li, and C. Wu, Phys. Rev. B **90**, 075114 (2014).
[9] C. Wu, Phys. Rev. Lett. **101**, 186807 (2008).
[10] H. Kontani, T. Tanaka, D. S. Hirashima, K. Yamada, and J. Inoue, Phys. Rev. Lett. **102**, 016601 (2009).
[11] S. Bhowal and S. Satpathy, Phys. Rev. B **101**, 121112(R) (2020).
[12] D. Go, D. Jo, C. Kim, and H.-W. Lee, Phys. Rev. Lett. **121**, 086602 (2018).
[13] K. S. Takahashi, M. Onoda, M. Kawasaki, N. Nagaosa, and Y. Tokura, Phys. Rev. Lett. **103**, 057204 (2009).
[14] K. S. Takahashi, H. Ishizuka, T. Murata, Q. Y. Wang, Y. Tokura, N. Nagaosa, and M. Kawasaki, Sci. Adv. **4**, aar7880 (2018).
[15] K. Ahadi, Z. Gui, Z. Porter, J. W. Lynn, Z. Xu, S. D. Wilson, A. Janotti, and S. Stemmer, APL Mater. **6**, 056105 (2018).
[16] J. P. Perdew, K. Burke, and M. Ernzerhof, Phys. Rev. Lett. **77**, 3865 (1996).
[17] P. Blaha, K. Schwarz, F. Tran, R. Laskowski, G. K. H. Madsen, and L. D. Marks, J. Chem. Phys. **152**, 074101 (2020).
[18] K. Maruhashi, K. S. Takahashi, M. S. Bahramy, S. Shimizu, R. Kurihara, A. Miyake, M. Tokunaga, Y. Tokura, and M. Kawasaki, Adv. Mater. **32**, 1908315 (2020).
[19] N. Marzari and D. Vanderbilt, Phys. Rev. B **56**, 12847 (1997).
[20] A. A. Mostofi, J. R. Yates, Y.-S. Lee, I. Souza, D. Vanderbilt, and N. Marzari, Comput. Phys. Commun. **178**, 685 (2008).
[21] X. Wang, J. R. Yates, I. Souza, and D. Vanderbilt, Phys. Rev. B **74**, 195118 (2006).
[22] J. Brous, I. Fankuchen, and E. Banks, Acta Crystallogr. **6**, 67 (1953).
[23] E. Stryjewski and N. Giordano, Adv. Phys. **26**, 487 (1977).
[24] H. Akamatsu, Y. Kumagai, F. Oba, K. Fujita, H. Murakami, K. Tanaka, and I. Tanaka, Phys. Rev. B **83**, 214421 (2011).
[25] T. Birol and C. J. Fennie, Phys. Rev. B **88**, 094103 (2013).
[26] J. H. Lee, X. Ke, N. J. Podraza, L. F. Kourkoutis, T. Heeg, M. Roeckerath, J. W. Freeland, C. J. Fennie, J. Schubert, D. A. Muller, P. Schiffer, and D. G. Schlom, Appl. Phys. Lett. **94**, 212509 (2009).
[27] T. R. McGuire, M. W. Shafer, R. J. Joenk, H. A. Alperin, and S. J. Pickart, J. Appl. Phys. **37**, 981 (1966).
[28] C.-L. Chien, S. DeBenedetti, and F. D. S. Barros, Phys. Rev. B **10**, 3913 (1974).
[29] T. Katsufuji and Y. Tokura, Phys. Rev. B **60**, R15021 (1999).
[30] T. Katsufuji and H. Takagi, Phys. Rev. B **64**, 054415 (2001).
[31] Z. Gui and A. Janotti, Phys. Rev. Lett. **123**, 127201 (2019).
[32] D. Bessas, K. Z. Rushchanskii, M. Kachlik, S. Disch, O. Gourdon, J. Bednarcik, K. Maca, I. Sergueev, S. Kamba, M. Ležaić, and R. P. Hermann, Phys. Rev. B **88**, 144308 (2013).
[33] A. Bussmann-Holder, J. Köhler, R. K. Kremer, and J. M. Law, Phys. Rev. B **83**, 212102 (2011).
[34] D. S. Ellis, H. Uchiyama, S. Tsutsui, K. Sugimoto, K. Kato, D. Ishikawa, and A. Q. R. Baron, Phys. Rev. B **86**, 220301(R) (2012).
[35] T. Zhao, L. M. Daniels, B. Slater, M. J. Rosseinsky, and F. Corá, J. Phys. Chem. C **124**, 13045 (2020).
[36] J. Son, P. Moetakef, B. Jalan, O. Bierwagen, N. J. Wright, R. Engel-Herbert, and S. Stemmer, Nat. Mater. **9**, 482 (2010).
[37] O. N. Tufte and P. W. Chapman, Phys. Rev. **155**, 796 (1967).
[38] S. Kobayashi, Y. Mizumukai, T. Ohnishi, N. Shibata, Y. Ikuhara, and T. Yamamoto, ACS Nano **9**, 10769 (2015).
[39] K. van Benthem, C. Elsässer, and R. H. French, J. Appl. Phys. **90**, 6156 (2001).
[40] R. Ranjan, H. S. Nabi, and R. Pentcheva, J. Phys.: Condens. Matter **19**, 406217 (2007).

[41] H. Uwe, R. Yoshizaki, T. Sakudo, A. Izumi, and T. Uzumaki, Jpn. J. Appl. Phys. **24**, 335 (1985).
[42] H. P. R. Frederikse, W. R. Hosler, W. R. Thurber, J. Babiskin, and P. G. Siebenmann, Phys. Rev. **158**, 775 (1967).
[43] G. L. Stamokostas and G. A. Fiete, Phys. Rev. B **97**, 085150 (2018).
[44] J. Muggli, Z. Angew Math. Phys. **23**, 311 (1972).
[45] K. M. Krishnan, *Fundamentals and Applications of Magnetic Materials* (Oxford University Press, Oxford, 2016).
[46] H. Kontani, T. Tanaka, and K. Yamada, Phys. Rev. B **75**, 184416 (2007).
[47] S. Bhowal and S. Satpathy, Phys. Rev. B **99**, 245145 (2019).
[48] M. Onoda and N. Nagaosa, J. Phys. Soc. Jpn. **71**, 19 (2002).